Ab initio modeling of nonequilibrium electron-ion dynamics of iron in the warm dense matter regime

T. Ogitsu, A. Fernandez-Pañella, S. Hamel, A. A. Correa, D. Prendergast, C. D. Pemmaraju, and Y. Ping

Phys. Rev. B **97**, 214203 — Published 11 June 2018

DOI: 10.1103/PhysRevB.97.214203

Ab-initio modeling of non-equilibrium electron-ion dynamics of iron in warm dense matter regime

T. Ogitsu[1], A. Fernandez-Pañella[1], S. Hamel[1], A.A. Correa[1], D.G. Prendergast[2], D. Pemmaraju[2], and Y. Ping[1]
[1] *Lawrence Livermore National Laboratory, Livermore, California 94550, USA*
[2] *The Molecular Foundry, Lawrence Berkeley National Laboratory, Berkeley, California, 94720, USA*

Spatiotemporal electron and ion relaxation dynamics of iron induced by femtosecond laser pulse was studied using one dimensional Two Temperature Model (1D-TTM) where the electron and ion temperature dependent thermophysical parameters, specific heat (*C*), electron-phonon coupling (*G*), and thermal conductivity (*K*), are calculated with *ab-initio* density-functional-theory (DFT) simulations. Based on the simulated time evolutions of electron and ion temperature distributions ($T_e(x,t)$ and $T_i(x,t)$), time evolution of X-ray Absorption Near Edge Spectroscopy (XANES) was calculated and compared with experimental results reported by Fernandez-Pañella *et al.* where the slope of XANES spectrum at the onset of absorption (*s*) was used due to its excellent sensitivity to the electron temperature. Our results indicate that ion temperature dependences on *G* and *C*, that are largely neglected in the past studies, are very important for studying non-equilibrium electron-ion relaxation dynamics of iron in warm dense matter (WDM) condition. It is also shown that 1/*s* behavior becomes very sensitive to thermal gradient profile, in the other words, to the values of *K* in TTM simulation, for the range of target thickness of about two to four times of the mean free path of conduction electrons. Our approach based on 1D-TTM and XANES simulations can be used to determine optimal combination of target geometry and laser fluence for a given target material that will enable us to tightly constraint thermophysical parameters under electron-ion non-equilibrium WDM condition.

I. Introduction

Recent development in time-resolved experimental measurement techniques made it possible to obtain the detailed information about the non-equilibrium material properties in warm dense matter (WDM) regime [1-5] that is realized in the time scale of about one picosecond. In particular, the approach of using a uniform slab of nanoplasma, produced by heating a thin foil with a fs laser [6, 7], has demonstrated that an accurate assessment of the thermophysical parameters such as electron-phonon coupling and specific heat under non-equilibrium WDM conditions ($T_e \sim$ eV; $T_e > T_i$) is feasible. [8-16]

Pioneering works of Ng *et al.* on measurements of time resolved optical absorption spectrum of gold demonstrated the temporal evolution of highly excited (~ a few eV/atom) electronic structure of metals can be observed with a time resolution of about 1 ps.[10, 11, 17] Subsequently, time resolved X-ray absorption spectroscopy (XANES) techniques have been used to determine the temporal evolution of electron temperature of copper [14, 16] and aluminum. [18] Unlike optical absorption spectroscopy where both the initial and final states of optical transitions are variables that are constrained by the energy conservation law, the initial state of a X-ray excited transition is fixed to the core-level and the spectral shape can be approximated by the projected density of states multiplied by the electronic occupation probability. *Accordingly, the onset of XANES for a metal shows a great sensitivity to the variation of electron temperature*. On the other hand, the use of XANES to determine the temporal evolution of the lattice temperature in WDM conditions is yet to be practical for the following two reasons: as the lattice temperature is raised, the XANES profile is smeared out [19] and the S/N ratio of the measurements deteriorates as a fine time resolution is required. Ultrafast electron diffraction (UED) measurements, on the other hand, are capable of providing the information about the time evolution of lattice structure and its thermal disorder as the Debye-Waller factor, from which, the lattice temperature could be estimated, albeit no information regarding the electron temperature can be directly obtained.[8, 12] In order to understand the overall system behavior (time evolutions of electron and ion temperature, $T_e(t)$ and $T_i(t)$) Two-Temperature-Model [20] (TTM) has been frequently used, where several thermophysical properties

such as electronic and lattice specific heat, electron phonon coupling, electronic and lattice thermal conductivities, in addition to the information about the initial condition (pump laser absorption profile) are required to define the time evolution of the electrons-ions system. Through these experimental studies, it has become clear that ab-initio derived thermophysical properties [21-23] provide good agreement on the evolution of electron and ion temperatures where the electron temperature dependence of the thermophysical properties become important for the temperature evolution profile. [12-16, 18, 24] It should be emphasized that the electron temperature affects the thermophysical properties in two different levels: the rigid band approximation can be used at modest electron temperatures where change of properties are well described by the change of electron occupation alone, [21, 22] while full self-consistent approach may be required at high electron temperatures where electron excitation significantly change the electronic structure as well as the mechanical property. [12, 16, 23]
Previous studies discussed so far relied partly on isochoric heating that was realized by choosing the target thickness thinner than the ballistic transport range of conduction electrons. [6, 7] This choice made it impossible to gain information regarding the thermal conductivity, while it simplified the analysis based on TTM model as the target does not develop thermal gradient.

In this study, we show how the thermophysical parameters, including thermal conductivity, for electron-ion non-equilibrium condition in WDM regime could be constrained based on a study using a similar system, however, by choosing the target thickness that is thicker than the ballistic transport range of electrons. Important factor will be the combination of target material, its thickness and the laser fluence that will maximize the effect of temperature gradient to the XANES spectrum. We will show how these parameters can be determined by the TTM-XANES simulations. It has been reported recently that reduction of G at the elevated electron temperatures is necessary for their experimental results to be consistent with the simulation results presented in this paper: [25] crucial evidence that supports validity of the Wang's G formula in WDM condition. [21] In this paper, we provide complete description of the computational procedure, detailed and systematic analysis on the simulation results, and assessments on the various factors that may affect on the simulation results.

In the following, we will first discuss about the our TTM (II-i), ab-initio MD simulations (II-ii) used to generate atomic configurations, with which we calculate, electron-phonon coupling (II-iii), specific heat (II-iv), and thermal conductivity (II-v). We will then review our results of TTM and of XANES simulations, where we discuss how the choice of G (electron-phonon coupling), C (specific heat) and K (thermal conductivity) affects on spatiotemporal (T_e, T_i) behavior, which in turn, results in significant difference in the time evolution of onset slope of XANES that is a reflection of the electron temperature distribution. At last, we summarize our results and discuss how our TTM-XANES simulation scheme could be used to help designing the experimental setting that will most effectively constraint the thermophysical parameters in electron-ion non-equilibrium WDM condition.

II. Method

II-i. Two-Temperature Model (TTM)

In this section, we describe about the TTM implementation developed for analyzing the experimental results reported in Ref [25]. The system of our interest is a thin slab of iron (d=60nm), whose electronic subsystem is excited to a few eV using a 150 fs pulse laser (400 μm). For a given laser pump energy, one can determine the absorbed energy by measuring the transmission and reflection. If the electronic specific heat is known, one can determine the initial electron temperature right after the laser excitation. The distribution of excess kinetic energy immediately after the optical excitation will exhibit an exponential

form reflecting the optical penetration profile, ~exp(-x/δ), where δ is the optical penetration depth and x is the position in the target measured from the surface (δ= 12nm for iron). The dynamics of electron and ion subsystems were then described within a TTM: excess kinetic energies of electrons and ions are interpreted as "temperature", the energy dissipations within the subsystems are described by classical heat transport, and the energy exchange between electronic and ionic subsystems is defined by the electron-phonon coupling factor, G. [20]

$$C_e \frac{\partial T_e}{\partial t} = \frac{\partial}{\partial x}\left(K_e \frac{\partial T_e}{\partial x}\right) - G \cdot (T_e - T_i) + S(x,t) \quad \text{eq. 1}$$

$$C_i \frac{\partial T_i}{\partial t} = \frac{\partial}{\partial x}\left(K_i \frac{\partial T_i}{\partial x}\right) + G \cdot (T_e - T_i) \quad eq.2$$

Here, C_e is the electronic specific heat, K_e is the electronic thermal conductivity, G is the electron-phonon coupling, S is the pump pulse, C_i is the lattice (or ionic) specific heat, K_i is the lattice thermal conductivity, T_e is the electron temperature, T_i is the ionic temperature and x is the position in the target. In this study, all of these parameters, *G, C, K* were calculated based on ab-initio DFT simulations. In the following, we will first describe how ab-initio MD simulations were performed, then explain how *G, C, K* were calculated using the MD simulation results, and how XANES spectrum was calculated for the system with large electron and ion temperature distributions.

We note that, in order to reduce computational complexity and cost, we did not use fully (T_e, T_i) dependent *G, C, K*. Instead we used T_e dependent G and C calculated at several T_i, and focused on understanding how the choice of T_i for *G, C* will affect on the simulation results of TTM as the (T_e, T_i) distribution as a function of time delay. For K, as discussed in section II-v, T_i dependency (or effect of electron-ion non-equilibrium) turned out to be marginal for iron so that it was therefore omitted in this study (electron-ion equilibrium value was used). Our intention is to provide all the necessary information for fully T_e, T_i dependent TTM-XANES simulations in this paper for future reference.

II-ii Ab-initio molecular dynamics simulations

Input parameters for TTM used in this study, such as specific heat and electron-phonon coupling, are given as ensemble average. Therefore, we first performed ab-initio molecular dynamics simulations at several temperature points at ambient pressure. Note that the same atomic configurations were used for the XANES simulations. For the electronic thermal conductivity calculations, additional MD simulations with larger system sizes were performed since the calculations of transport properties, such as thermal conductivity or electric conductivity, tend to be more sensitive to the simulation size than, for example, EDOS, which is used to estimate G and C.

In order to sample relevant phases of iron, T=300K (ferromagnetic bcc phase), T=1000K (fcc phase), and T=2000K, 5000K, 10000K, 20000K, 30000K (liquid) were chosen. We note that for the MD simulations, we assumed T_e=T_i in this study as our scope is rather to probe the extent of applicability of our approach, and leave full T_e, T_i dependent simulation for future investigations. PAW approach implemented in VASP was used with the planewave cutoff energy of 321 eV (we used the Fe_GW 2010 PBE PAW potential from the VASP library). We use the (1/4,1/4,1/4) K-point, and the PBE approximation of the exchange-correlation functional. The bcc, fcc, and liquid MD simulations were performed with the simulation box size of 64, 54, and 64 atoms, respectively, for G and C calculations. For the calculations of thermal conductivity, size effect is known to be relatively large, [26-28] therefore, we have used larger supercell permissible for a given temperature (up to 250 atoms) in order to assess and to correct the size effect. Note that the number of balance bands required for high temperature simulations increases due to the Fermi occupations leading to higher simulation cost, which limit the simulation size more than at low temperature.

For each case, total simulation time of about 10 ps with time step Δt = 2fs was performed, and 50 snapshots were chosen randomly from the last 8 ps of the simulations and used for the rest of the calculations.
We note that ab-initio MD at T=300K (bcc structure) was performed with spin polarization, however, *G*, *C* and *K* were calculated without spin polarization using the atomic configurations obtained with spin polarization. This is because strong optical excitation is known to suppress ferromagnetism of transition metals such as iron instantaneously. [29-48] Accordingly, nonmagnetic electronic structure was assumed for the calculations of *G* and *C* at *T*=0K as well.

II-iii Electron-phonon coupling constant, *G*

For the electron (and ion) temperature dependent electron-phonon coupling parameter, we used the formula developed by Wang *et al*.,[21] which is a high temperature approximation of the original formula derived by Allen.[49]

$$G = \frac{4\pi}{\hbar V}\sum_{k,k'}|M_{kk'}|\,S(k,k')\delta\left(\varepsilon_k - \varepsilon_{k'} + \hbar\omega_Q\right) \qquad eq.3$$

here, $\hbar$ is Planck constant, V is the volume of the system, $|M_{kk'}|$ is the electron-phonon transition matrix element, S(k,k') is the statistical occupational probability distribution, which is,

$$S(k,k') = f_k(1-f_{k'})\eta_Q - f_{k'}(1-f_k)(\eta_Q+1) \qquad eq.4$$

here, f is the Fermi distribution function, η is the Bose distribution function. δ is delta function, ε_k and $\varepsilon_{k'}$ are the Kohn-Sham eigenvalues at the wave vectors, k and k', and $\hbar\omega_Q$ is the phonon energy at the phonon wave vector Q. When the electron temperature is significantly higher than the Debye temperature, one may use high temperature expansion that leads to the following expression found in Ref [21] (double sum on k, k' is replace by derivative with respect to energy using $\varepsilon_{k'} - \varepsilon_k = \hbar\omega_Q \ll k_B T_e$), which was used by *Lin et al*. to calculate *G* profiles of various metals. [22]

$$G_{T_i}(T_e) = \frac{\pi\hbar k_B \lambda\langle\omega^2\rangle}{n_{T_i}(E_f)}\int_{-\infty}^{\infty} dE\; n_{T_i}^2(E)\left(-\frac{\partial f((E-\mu)/k_B T_e)}{\partial E}\right) \qquad eq.4$$

where, k_B is Boltzmann constant, λ is the electron-phonon mass enhancement parameter, $<\omega^2>$ is the second moment of the phonon spectrum defined by McMillan (see Ref [21] for more detail), E_f is the Fermi level at T_e=T_i, $n_{Ti}(E)$ is the ensemble averaged electronic density of state calculated at T_i, μ is the chemical potential for a given T_e (> T_i) determined with the charge neutrality condition for a given $nT_i(E)$.

In this formula, the ion temperature dependence is included in EDOS, $n_{Ti}(E)$, which is calculated as ensemble average of instantaneous EDOSs obtained from ab-initio MD simulations. *G* values calculated at T_i=0K, 300K, 2000K, 5000K and 10000K are depicted as Fig. 1 (right).

II-iv Electronic specific heat

The electronic specific heat was calculated using

$$C_e(T_i, T_e) = \frac{\partial E(T_i, T_e')}{\partial T_e'}|_{T_e'=T_e} \qquad eq.5$$

In principle, one can explicitly calculate ab-initio $E(T_i, T_e)$ on (T_i, T_e) grid points, interpolate the table and perform numerical derivative with respect to T_e at a given (T_i, T_e). Here, $E(T_i, T_e)$ is ensemble average of instantaneous internal energies obtained from ab-initio MD. Alternatively, one can use the formula for temperature dependence of internal energy based on electronic density of states (EDOS), and calculate the specific heat using the above formula. In this case, we may perform the ab-initio MD on T_i grid, where $T_i=T_e$ is assumed. This corresponds to the rigid band approximation. The accuracy of this approximation was accessed for limited cases (see Fig. 1), which indicated that the electronic relaxation effect decreases as ion temperature rises. In this study, we used the C values obtained with the rigid band approximation as below.

$$E(T_i, T_e) = E_0 + \int_{-\infty}^{\infty} dE\ (E - E_f) f\left(\frac{E-\mu}{k_B T_e}\right) n_{T_i}(E) \qquad eq.6$$

where, E_f is the Fermi level at $T_e=T_i$, $n_{T_i}(E)$ is the ensemble averaged electronic density of state calculated at T_i, μ is the chemical potential for a given T_e (> T_i) determined with the charge neutrality condition for a given $n_{T_i}(E)$. E_0 is chosen in such a way that $E(T_i, T_e)$ becomes equivalent to the ensemble averaged internal energy, E_{DFT}, at T_i (= T_e). The electronic specific heat is then calculated using eq. 4 for the bcc structure with nonmagnetic state as well as for the MD trajectories simulated at four different ion temperatures, 300K, 2000K, 5000K, 10000K (see Fig. 1 left).
The lattice specific heat used in TTM simulations was calculated based on the Debye model with Debye temperature θ_D= 470 K.

II-v Thermal conductivity

Thermal conductivity as a function of temperature were calculated as follows. Using the atomic configurations generated by ab-initio MD (described in section II-ii), thermal conductivity of iron was calculated based on Chester-Thellung-Kubo-Greenwood formula in PAW formula. [50-52] Details of this formalism and its implementation are found in Ref [52]. This method has been used to calculate thermal conductivity of liquid Na, [27] Al, [52] and Fe, [28] and have shown good agreement with experimental data. We note that this approach does not use any kind of adjustable or empirical parameters such is the case with Wiedmann-Franz law. The calculated electron-ion equilibrium thermal conductivity together with the reported theoretical [28] and experimental [53, 54] data are shown in Fig. 2. Our results show a great agreement with the ab-initio results reported in literature [28] as well as the experimental values for $T > T_{melt}$, however, underestimate the experimental values at lower temperature, presumably due to lack of accurate lattice phonon contribution in solid state.
We have also investigated on effect of electron-ion non-equilibrium for limited cases (Fig 3). We chose T_i=2000K and T_i=10000K as representing cases as our TTM simulation results indicate that large portion

of the iron target will likely to stay in this temperature range for the relevant duration for our analysis (t<5ps) for high fluence experiments. As one can see, non-equilibrium effect on thermal conductivity is relatively small, particularly for liquid iron. Accordingly, we used the electron-ion equilibrium values for our TTM simulations, where linear interpolation was used to obtain the electron thermal conductivity values for an arbitrary electron temperature.

The precise lattice thermal conductivity values of iron are not known for the temperature range of our interest, however, general trend is known to behave as follow. The lattice thermal conductivity in solid state is known to show maximum below the Debye temperature (θ_D) then rapidly decrease due to exponential increase in the frequency of Umklapp processes with rising temperature to well above θ_D. [55] In our study, the lattice thermal conductivity was chosen to be $K_i/K_e = \sqrt{m_{Fe}/m_{ele}} \sim 1/100$, where m_{Fe} is the atomic mass of iron and m_{ele} is the mass of electron. This choice may be reasonable for high temperature (T > 2000K), however, it is likely to be significantly underestimated in the solid phases. Nevertheless, with the current experimental time resolution of about 2.5ps, error in $1/s$ stemming from the error in K_i is unlikely to be significant compared to the experimental error bar as our TTM analysis indicates that T_i could exceed the melting temperature in a fraction of picosecond where our approximation on K_i will become justified.

Another factor that was considered for the thermal conductivity values for our TTM simulations is the polycrystalline nature of the target thin film used in Ref [25]. It has been known from 1970s that fine-grained poly crystalline materials tend to show lower thermal and electric conductivities than those of single crystals, presumably due to scattering at the grain boundaries and/or at the surface (note: nanometer scale thin films tend to become polycrystalline). [56-58] A few models were developed to account for the reduction of transport properties due to the additional scattering sources: Fuchs-Sondheimer (FS) model[59] for the surface scattering and Mayadas-Shatzkes (MS) model [57, 58] for the grain boundary scattering. Further studies in the past two decades demonstrated that (a combination of) these models qualitatively reproduced the transport behavior of various materials (Cu, [60, 61] Au, [61-65] Pt, [66, 67] Ni, [68, 69] Al, [61] Ir [70]) for wide ranges of film thicknesses and/or grain sizes. In our study, only the MS model was used to estimate the thermal conductivity of the polycrystalline iron thin film (60 nm) used in Ref [25] for the following reasons: The mean free path of conduction electrons of iron (~10 nm) is significantly shorter than the film thickness (60 nm) so that the surface scattering effect is expected to be marginal, while the target iron film used in Ref [25] has a relatively fine grain size of 10 nm that is about the same with the mean free path, [71-73] which is likely to affect the thermal conductivity significantly. The formula (MS model) and the parameters values used in our study are as follows. [57, 58]

$$\frac{K_{pc}}{K_{sc}} = 3\left[\frac{1}{3} - \frac{\alpha}{2} + \alpha^2 - \alpha^3 \ln\left(1+\frac{1}{\alpha}\right)\right] \;\; ; \;\; \alpha = \frac{l}{d}\frac{R}{1-R} \;\; , \qquad eq.7$$

where l is the mean free path of conduction electrons in single crystal material, d is the grain size, and R is the grain boundary reflection coefficient. In our case, l = 10 nm, [71-73] d = 10 nm, [25] and R = 0.25 were used. We note that information regarding the R for polycrystalline thin iron film is not available in literature, and our choice of R = 0.25 was based on the study on Au thin film. [62] More discussions on the sensitivity of this value to the onset slope of XANES spectrum will be found later. Regarding R value for Fe in literature, there is at least one experimental report on the effect of grain boundaries on the electric resistivity of iron, [74] however, Mayadas and Shatzkes did not report the R value for iron due to complications in interpreting the results, which are stemming from the magnetism of iron. [57] We emphasize that, although the accurate value of R for iron is not known, a poly crystalline iron must show lower thermal conductivity than that of a single crystal due to the grain boundary scattering. Given that the reduction observed in the other metals were not negligible (a few tens of percent), this effect was

taken into consideration. Accordingly, we tentatively used the R value estimated for Au, and leave the accurate determination of the scattering parameter of iron for future investigations.

II-iii. X-ray absorption spectrum calculations

For the atomic configurations generated by the ab-initio MDs described before, the electronic structures were calculated using PWSCF code in Quantum-Espresso package version 5.0, [75] together with the ultra-soft pseudopotential for Fe ion and the planewave cutoff energy of E_{cut}=40 Ry and the charge density cutoff energy of E_{cut} = 300 Ry. PBEGGA exchange-correlation potential was used to describe the many body effect of electrons. [76] For the ground state, and core-excited states self-consistent total energy calculations, 32 k-points on a regular grid were sampled.

For the final states of the dipole transition matrix elements, excited-core-hole (XCH) was used. [77] The electron temperature dependent dipole matrix elements were then calculated using the Kohn-Sham wavefunction obtained for the given electron temperature. In order to achieve a numerical convergence in integrating the Brillouin Zone, the Bloch state based interpolation schemed described in ref [78] was employed with about 8^3 (16^3) k-point grid density for the bcc and liquid (fcc) simulations.

$$I(E) = 4\pi\alpha_0 E \sum_f \left|\langle\Psi_f|\hat{\mathcal{E}}\cdot R|\Psi_i\rangle\right|^2 \left(1 - f\left(\frac{E-E_f}{k_B T}\right)\right)\delta\left(E_f - E_i - E\right) \qquad eq.8$$

Once dipole matrices were generated for each snapshot, the self-consistently determined Fermi distribution function *(1-f)* is multiplied, then, the excitation lifetime broadening (Lorentzian) in the energy dependent form, [79-81] Gaussian broadening with σ_{FWHM}=0.3eV corresponding to the detector resolution, were applied. When the ensemble average of the *I(E)* over the atomic configurations were taken, the chemical shift was taken into consideration using the final state theory (complete screening), which is based on energy conservation law. [82] Alternatively, one may calculate the core-level shift as a perturbation from surrounding atoms to the core-level of interest. [83] According to the final state theory, the shift of core-level (E_{CLS}) is defined as follow.

$$E_{CLS} = \left(E'(N-1) - E'(N)\right) - \left(E_{ref}(N-1) - E_{ref}(N)\right) \qquad eq.9$$

Here, a core-hole pseudopotential (one electron is removed from the core-level of our interest) is used to calculate *E(N-1)* while *E(N)* is calculated with a neutral pseudopotential. This information is used in two ways. One is when taking an ensemble average for a fixed (T_i, T_e), where E_{CLS} between different atomic configurations is estimated based on this formula. The other is to adjust the reference energies between different (T_i, T_e)s, where the ensemble averaged $\langle E_{CLS}\rangle$ for given (T_i, T_e)s are calculated. Here, $E_{ref}(N)$ and $E_{ref}(N-1)$ are calculated at T_i=T_e=300K, and $E'(N)$ and $E'(N-1)$ are the ones calculated at different T_i and T_e. The former will contribute to thermal broadening of XANES as a combined effect with the fluctuation of dipole matrix due to thermal fluctuation of ion configurations. In the other words, thermal broadening in our XANES is directly taken into consideration as the ensemble averaging. We note that one may use the approach based on quasi harmonic approximation for ensemble average of solid phases particularly if quantum zero-point motion is important, in the other words, accurate XANES profile in a solid phase is necessary. [84]

In this way, we obtained ensemble averaged $\langle I(E)\rangle$ on the two-dimensional (T_i, T_e) grid points. We then calculate $I(E,t)$ for a given delay time using the $T_i(x,t)$, $T_e(x,t)$ profile calculated with the TTM, we used a linear interpolation of $\langle I(E)\rangle$ on the (T_i, T_e) grid on which the ab-initio MD simulations were performed, and for each T_i, $T_e = T_i + n\ \delta T$ where δT=5000K and n = 0, *nmax* where *nmax* is chosen such a way that

maximum T_e exceed the maximum temperature observed in the TTM simulation. In our case, the maximum T_e of 70000K was taken in order for the grid space to cover the temperature range that was estimated for the highest fluence experiments using C_e and the energy deposition profile based on the optical penetration depth of iron.

$$I(E,t) = \int_{x_0}^{x_{max}} dx \, \langle I(E) \rangle_{T_i(x,t),T_e(x,t)} \qquad eq.10$$

At last, Gaussian convolution along time axis with σ_{FWHM}=2.5ps is applied in order to reflect the detector time resolution of 2.5ps.

We note that, in this study, we only use Fe L_3 edge XANES and L_2 edge is omitted. This is because we are only using the onset slope of XANES in order to investigate on electron and ion temperature distribution in the target, and the level splitting of Fe *2p* levels due to spin-orbit coupling, $E_{2p3/2}$ (L_3 edge) – $E_{2p1/2}$ (L_2 edge), is larger than 10 eV, [25] in the other words, the contribution of L_2 edge to the onset slope is negligible.

III. Results and discussions

Let us first discuss about the TTM simulation results that are obtained with a set of thermophysical parameters (*G* and *C*) derived at different T_i (T_i=T_e is assumed for *K* due to the marginal non-equilibrium effect observed within our approach).

Let us first briefly review important features in *G* for TTM simulations. *G* value start at a relatively high value at low temperature, which decreases as the electron temperature rises, and the overall values are decreased as ion temperature is increased where the extent of reduction is larger for low ion temperature (or in solid state, T < 2000K). See Figure 1 (right). A careful examination of the formula (eq. 3) gives a clear explanation of this behavior, which motivated the series of studies [14, 16] including the current study. In essence, the kernel of integration in eq. 3 is the product of square of EDOS and a Gaussian centered at the Fermi level whose width is k_BT. Accordingly, its integrated value is dictated by the number of states within k_BT near the Fermi level. Now, the EDOS of iron, if one assumes nonmagnetic state, has a large *d*-band peak at around the Fermi level whose half width is about one eV. This is responsible for the declining $G(T_e)$ of iron: as the electron temperature (or k_BT value) increased compared to the width of *d*-peak, average number of states in EDOS within k_BT decreases. Accordingly, *G* value decline as a function of T_e as well. When ion temperature is raised, the *d*-peak is broadened due to thermal fluctuation of ions and this leads to downward shift of *G* curve.

The experimental condition used in Ref [25] was set to bring the target to WDM condition by choosing the laser fluence so that the final (equilibrium) temperature will become on the order of one eV, where the tamping layers were used to delay target expansion for the duration of our interest (up to several ps). The details about the setting and the assessments are found in Ref [25].

In this study, we used the experimentally determined value of the energy absorbed by the target, 0.95 (Jcm^{-2}).

The resultant T_e, T_i profiles as a function of position at *t=0.5, 2.5, 5.0, 7.5* and *10.0 ps* with (*G*, *C*)s for T_i *= 0, 300, 2000, 5000, 10000 K* are shown as Fig. 4. There are two features that are notable in these T_e, T_i profiles: electron-ion temperature difference and extent of thermal gradient.

First, at *t = 0.5 ps,* the electron-ion temperature difference, $T_e - T_i$, for $(G,C)_{T_i=0K}$ is smallest in the back side of target (ex. *x > 20 nm*), where both T_e and T_i are relatively low compared to the front side of target reflecting of large *G* at low T_i and T_e (Fig. 1). In general, T_e – T_i, is smaller for (*G, C*) calculated at lower

T_i, which is explained by the G profiles: lower the T_i, higher the G values (faster energy transfer from electrons to ions), which will translate to smaller $T_e - T_i$ for G calculated at lower T_i.
Second, the temperature gradient (or difference in front and back temperatures) remains larger for larger G values (i.e. G calculated with lower T_i). This is explained by larger electronic thermal conductivity than ionic thermal conductivity in addition to the role of G values discussed above: larger G values at low T_i (and T_e), which is the back side of target and it is particularly the case for early time delay, will reduce the electron temperature. This behavior is particularly pronounced when $G_{T_i=0K}$ is used for the TTM simulation where lower electron temperature due to larger G values will lead to slower heat diffusion in the target due to $K_e >> K_i$.

Using these electron and ion temperature profiles, $T_e(x,t)$ and $T_i(x,t)$, we calculated XANES spectrum as function of both target position and delay time. The spatial average of the spectrum over the target is then performed as shown in Figure 5. As one can see, the XANES profiles at the front and back side of target are dramatically different reflecting the large difference in (T_e, T_i)s, which strongly indicates the importance of averaging procedure developed in this study. The spatially averaged XANES profiles as a function of delay time is then convoluted with Gaussian function with $\sigma_{FWHM} = 2.5ps$ in order to take the experimental detector time resolution into consideration.[25] See Fig. 6 for the resultant XANES profiles that were calculated with $(G, C)_{T_i=10000K}$ and K_{pc}.

Let us now compare our simulation results and the experimental results reported in Ref [25]. In performing the comparison, we used onset slope of XANES profiles as it has shown great sensitivity to the electron temperature in the previous studies. [14, 16, 18] For both experimental and theoretical results, the slope, s, was calculated at the half of peak, where the peak height was normalized to one in order to have a consistent definition. Resultant inverse of slope, $1/s$, calculated with series of (G, C)s together with the experimental results reported in Ref [25] are found in Fig. 7. We note that we chose $1/s$, not s, for an intuitive presentation since $1/s$ (s) is increasing (decreasing) function of electron temperature.
As one can see, largest difference in $1/s$ profiles are seen at about t=2.5 ps where $1/s$ value is higher for lower G value, which is due to competition between electronic heat diffusion and energy transfer from electrons to ions: larger G value leads to faster cooling of electrons, which leads to smaller $1/s$. At this delay time, blue and green lines are within the experimental error bar, while their difference is about the size of error bar (Fig. 7). This is to some extent surprising given the relatively small difference in G and C calculated at Ti=5000K and 10000K (Fig. 1), and the small difference in corresponding $T_i(x,t=2.5ps)$ and $T_e(x,t=2.5ps)$ profiles (blue and green) seen in Fig. 4. We here emphasize the implication of these observations: *our approach described in this paper and in ref [25] is capable of constraining the thermophysical parameters of materials in electron-ion nonequilibrium WDM condition very tightly*, which will be briefly discussed as follows.

The most important concept is constraining G, C, K based on the approach discussed in this paper is that relative contributions of (G, C) and K to $1/s(t)$ varies significantly for a certain range of target thickness (and the pump laser fluence). The range of target thickness can be estimated based on the mean free path of the conduction electrons of the target material. When the target thickness is close to the mean free path, the electron temperature will achieve (near) homogeneous distribution rapidly. In this case, thermal conductivity does not play a role in the electron-ion relaxation dynamics. As the target thickness is increased, larger inhomogeneity will be sustained for a longer duration, where the contribution of K to the relaxation dynamics will be increased. However, if the target is so thick so that the major portion is cold, information of temperature distribution in $1/s(t)$ will diminish (or dominated by the cold part). Therefore, it is natural to expect that there will be an optimal range of thickness, where sensitivity of K to $1/s$ will be maximized. Accordingly, we have performed TTM simulation for the target thickness d = 20 nm, 40 nm, 60 nm and 80 nm assuming the same energy density deposited by the pump laser. The electron and ion

temperature distributions at four delay times are shown in Fig. 8 and the corresponding *1/s(t)* profiles are shown in Fig. 9.
With d = 20 nm target, homogeneous temperature distribution can be achieved by *t=2.5ps*. All the rest of target thicknesses exhibit inhomogeneous temperature distribution but with the degree proportional to the target thickness. *1/s(t)* profiles clearly reflect the extent of inhomogeneous temperature distributions in these cases (Fig. 9). We have also examined the effect of thermal conductivity to *1/s(t)* by changing the K values by $\pm 20\%$ (dashed lines). There is virtually no impact of changing K by 20% with d = 20 nm since the temperature distribution is already almost homogeneous, while the change in 1/s can be seen clearly for larger d and, with d = 60 nm, the variation become much larger than the experimental error bar suggesting that constraining K value within 20% is feasible even with the current level of experimental uncertainty. These examples clearly demonstrate that one can constraint thermophysical parameters in electron-ion non-equilibrium WDM condition by performing time resolved XANES measurements for optimally chosen target geometry combined with appropriate pump laser fluences.

Let us now briefly review previous studies on electron-phonon coupling under electron-ion nonequilibrium condition. In 2008, based on DFT calculations, Lin *et al.* reported the thermophysical parameters of various types of metals, free electron like metal (Al), noble metals (Ag, Cu, Au), and transition metals (Ni, Pt, W, Ti), where the T_e dependent G were calculated based on the Wang's formula. [21, 22] The T_e dependence of G is expressed as an integeted value of the function that is a product of square of EDOS and energy derivative of the Fermi distribution (see eq 5) reflecting the few constraints in the original formula: a transition between electronic states is permitted only from an occupide state to an unoccupied state due to the Pauli exclusion principle and the energy and momentum conservation laws in an electron-phonon scattering event must be satisfied. Since the energy derivative of the Fermi function has a Gaussian like shape with about the width of k_BT the G profile becomes proportional to the number of available electron-electron transition channels within k_BT around the Fermil level. Accordingly the behavior of G for various metals can be qualitatively described as follows: G_{Al} is a linear function of temperature as EDOS does not change significantly at around the Fermi level. $G_{noble\ metal}$ will show sharp upturn as k_BT increases and *d*-to-*s/p* transitions become possible. $G_{transition\ metal}$ may start with a large value at low T reflecting the large d-EDOS then decrease rapidly as k_BT rises and the electron-electron transitions begins to include the lower density s/p-bands (Ni, Pt). However, if *d*-DOS exhibits a deep valley where the Fermi level is located, it may rather show sharp upturn as the peaks of d-EDOS gets within k_BT (W). We note that the above argument is justified only when $T_e >> \theta_D$ where the details about phonon-phonon scattering becomes less important. In case of iron, it is clearly seen that T_e dependence of G is crucial (see Fig 1). In addition, T_i dependence on G appears to be also important for relatively low T_i, particularly below the melting temperature. For Cu, the studies by Cho *et al*. using time resolved XANES measurements indicated that the electron temperature profile of G is similar to the one reported by Lin *et al*. However, in detail, their values at high electron temperature is higher than the Lin's G, then it saturates rapidly and crosses the Lin's G. Interestingly, the experimental values of G approaches to the theoretical G calculated with the high T_i liquid EDOS suggesting that T_i dependence, in addition to T_e dependence of G is important for Cu as well. [14, 16]
For Au, the situation is not as clear since the sets of experiments by two independent groups led to different conclusions regarding temperature dependence of G. An earlier study based on ultrafast electron diffraction experiments [12] showed that T_e dependent G combined with T_e dependent θ_D, [85] successfully reproduced the measured time scale of thermal lattice disordering. The later studies based on time resolved optical absorption measurements at $\hbar\omega$=1.55eV showed that use of relatively low constant G (2.2×10^{16} W/m^3/K) led to the best agreement with the experimental absorption time profile albeit only for high laser fluences.[15, 24] Note that the optical absorption of Au at $\hbar\omega = 1.55eV$ at low temperature consists of interband transitions, which is likely to be sensitive to T_i. For example, in case of Al, it was reported that the interband transition peak exhibits a very strong T_i dependence, [86] a factor that was not taken into consideration in these studies.

The studies on Cu and Fe using time resolved XANES indicate that both T_e and T_i dependence on G and C are important, however, given the controversial situation for Au, further systematic studies will be necessary for establishing temperature behavior of G of metals and its underlying factors in non-equilibrium WDM condition. The predominant factor of T_e dependence on G is the number of states within k_BT near the Fermi level, while the change of T_i modulates EDOS profile, which in turn, changes the number of states within k_BT near the Fermi level. We may suggest that such an electronic relaxation effect may be measured by the time resolved photoemission spectroscopy [87, 88] albeit the detection method that addresses the space charge effect need to be developed for WDM research.

We now turn our attention to the other important issues in understanding electron-ion dynamics in non-equilibrium WDM condition that were not considered in this study due to resource and time limitation: electron-phonon coupling in non-thermal distribution and mode dependent electron-phonon coupling.
Recently, it has been reported that non-thermal electron distribution that is presumably present in a very short time scale, significantly shorter than the time resolutions of any of experimental studies discussed above, would result in G profile that could be significantly different from that for thermal electron distribution (the Fermi distribution). Mueller and Rethfeld used "complete Boltzmann collision integrals" approach and calculated G as a function of absorbed laser energy with non-equilibrium and equilibrium electron occupation distribution for Al, Au, Ni. [89] The G profiles for Al and Au showed similar trend, i.e. an increasing function of T_e, for both equilibrium and non-equilibrium cases and, in WDM condition (T_e>10000K), they approach to the G_{Lin} profiles. However, for Ni, dramatically different behaviors to the G_{Lin} profile were observed regardless of the choice of occupations. With the equilibrium occupations approximation, the G curve is located significantly higher (about factor 5), though the profile is similar to the G_{Lin} (a similarly increasing function of T_e). On the other hand, the G profile for the non-equilibrium occupation becomes an increasing function of T_e. Although there is no comparable experimental result to these theoretical predictions partly due to the current limit of detector time resolution, it is a very important issue that needs to be examined by experiments in future.
Yet another interesting study on $G(T_e)$ profile of a metal was reported, which concerns phonon mode dependent G. Waldecker *et al*. performed femtosecond electron diffraction experiments on aluminum, and calculated the time evolution of lattice temperature from the decays of a few Bragg peaks. [90] For the TTM type analysis, they used G that has an explicit energy dependence of electron-phonon scattering efficiency via the Eliashberg function, which was omitted in the Wang's approximation. Naturally, their TTM formula takes thermal occupation of phonons into consideration, which means that their formula has an explicit lattice temperature dependency on G (and $C_{lattice}$) albeit within a linear perturbation theory. They argued that the discrepancy between their own calculations of G and experiments are due to differences in electron-coupling efficiency between different phonon modes, [91-96] and introduced the model where each phonon mode is treated as an independent degree of freedom, and called it Nonthermal Lattice Model or NLM. The NLM model showed an excellent agreement with the experiments for the final lattice temperature range of about θ_D of Al (433K), providing a deep insight into the detail of electron-phonon coupling behavior in condensed matter conditions. The question as to how the electron to lattice energy dissipation behavior will change (or not change) for higher laser fluence, within WDM conditions, will be of great interest to both condensed matter and warm dense matter research communities. Very interestingly, their experimental G profile agrees well with the Lin's G. Since our calculations of G are based on the same formula, we expect that our interpretations are not affected by the mode dependency discussed in their study. Nevertheless, further investigations on this aspect for non-equilibrium WDM iron is highly desirable in light of this report. [90]

At last, we discuss about an assumption that was necessary for the TTM and XANES simulation practically feasible, which is related to the role of magnetism to the phase stability of iron. It is known that iron takes ferromagnetic state with bcc crystal structure at ambient condition. [97-99] Using DFT calculations, it has been shown that fcc crystal structure becomes more stable than bcc if nonmagnetic electronic structure is used (spin polarization is turned off). On the other hand, it has been known that

intense optical pulse excitations of ferromagnetic systems such as iron, cobalt and nickel show ultrafast demagnetization. [44-48] Accordingly, we used nonmagnetic EDOS of iron to derive the thermophysical parameters such as C_e, and G.

This situation raises question regarding structural information of our target before it melts. In this study, we used the following two hypothetical scenarios. First one is to assume that the lattice structure stays bcc, while the electronic structure instantaneously transforms into the nonmagnetic state. Then, as the ion temperature rises, the lattice structure follows the known iron phase diagram: bcc-fcc transition at about the Curie temperature [97, 98] and eventually melts at the melting temperature. Second scenario: the loss of FM state leads to (near) instantaneous structural transition to fcc phase, then it melts at the melting temperature.

The calculated $1/s$ curves for these hypothetical models were noticeably different at around the initial peak, however, once the time convolution with σ_{FWHM}=2.5ps (the detector time resolution broadening) is applied the difference became negligible. Therefore, in this study, we tentatively adopted to the first scenario about the structural transformation, which is nonmagnetic bcc → nonmagnetic fcc → liquid. We hope that future experiments with higher time resolution will make it possible to discriminate these scenarios, and further provide a deeper insight into the nature of non-equilibrium phase transitions induced by optical excitation.

Summary

The procedure to simulate relaxation behavior of XANES spectrum of an iron thin film exposed to a femtosecond laser pulse is outlined in this paper, where the time evolution of spatial distribution of T_e and T_i are obtained using the ab-initio derived 1D-TTM model. *The results shown in this paper evidence that the proposed theory-experiment coupled approach is capable of constraining thermophysical properties of materials under electron-ion non-equilibrium WDM condition*. The crucial point in the experimental design is the choice of target thickness for a given material, which is slightly larger than the ballistic electron transport range so as to maximize sensitivity of electron and ion relaxation dynamics to thermal conductivity values. In designing such an experiment, one may also consider the change in ballistic range as a function of laser fluence as it was demonstrated that the ballistic range of gold is significantly reduced in WDM condition than that in condensed matter conditions, [100] which is consistent with the excitation energy dependence of mean free path determined by electron escape length measurements. [81]

Acknowledgment

The authors thank the stimulating discussions with Phil Heimann, Byoung-ick Cho, Lorin Benedict, Kyle Engelhorn, Andrew Ng, and Phil Sterne. This work was performed under the auspices the U.S. Department of Energy under contract No. DE-AC52-07NA27344, and supported by DOE HEDLP program.

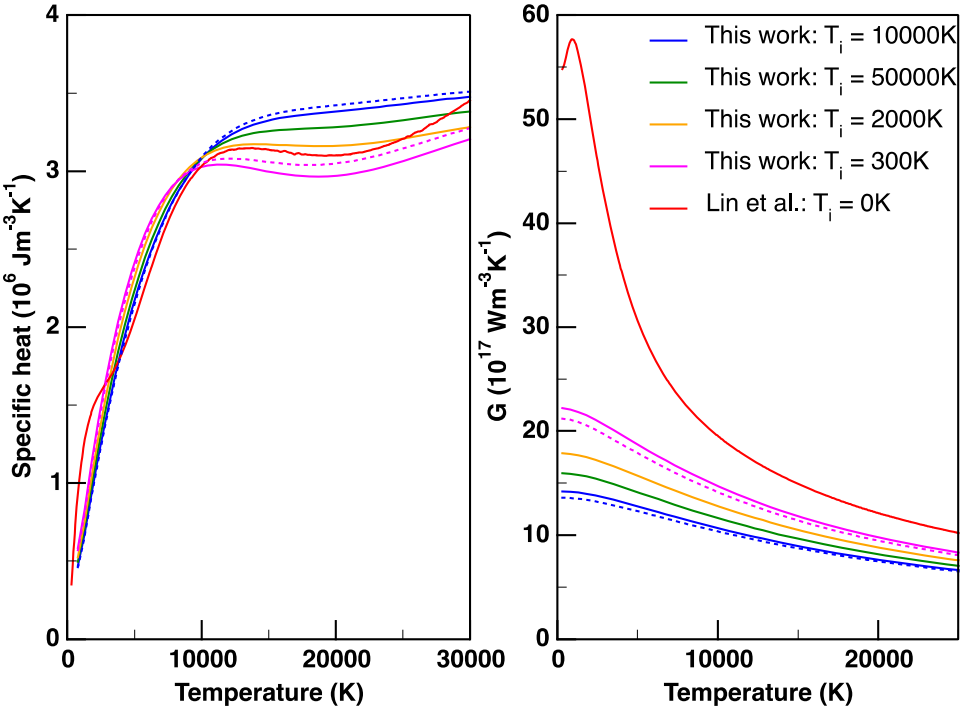

Figure 1: Specific heat and electron-phonon coupling parameter calculated as a function of T_e at different ion temperatures. The data of Lin *et al.* was calculated for perfect bcc crystal at $T=0K$, while the rest are ensemble averaged values based on ab-initio MD simulations. All the solid lines are obtained based on EDOS self-consistently calculated as $T_e=T_i$, while dashed lines are obtained based on EDOS self-consistently calculated as $T_e=T_i$+20000K in order to assess the accuracy of rigid band approximation.

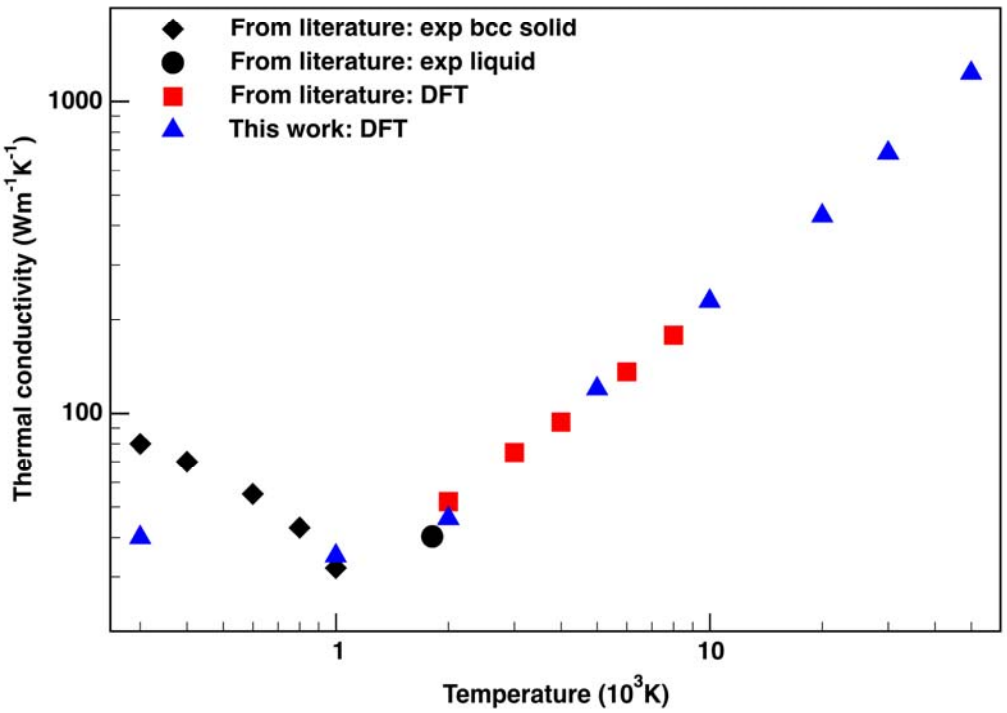

Figure 2: Thermal conductivity of iron calculated by ab-initio method described in the text (solid triangles for this work and solid squares for literature [28]) as well as experimental values for bcc solid (solid diamonds) [53] as well as for liquid (solid circle). [54] Our simulation results in this figure is calculated for electron-ion equilibrium (T_i=T_e) condition.

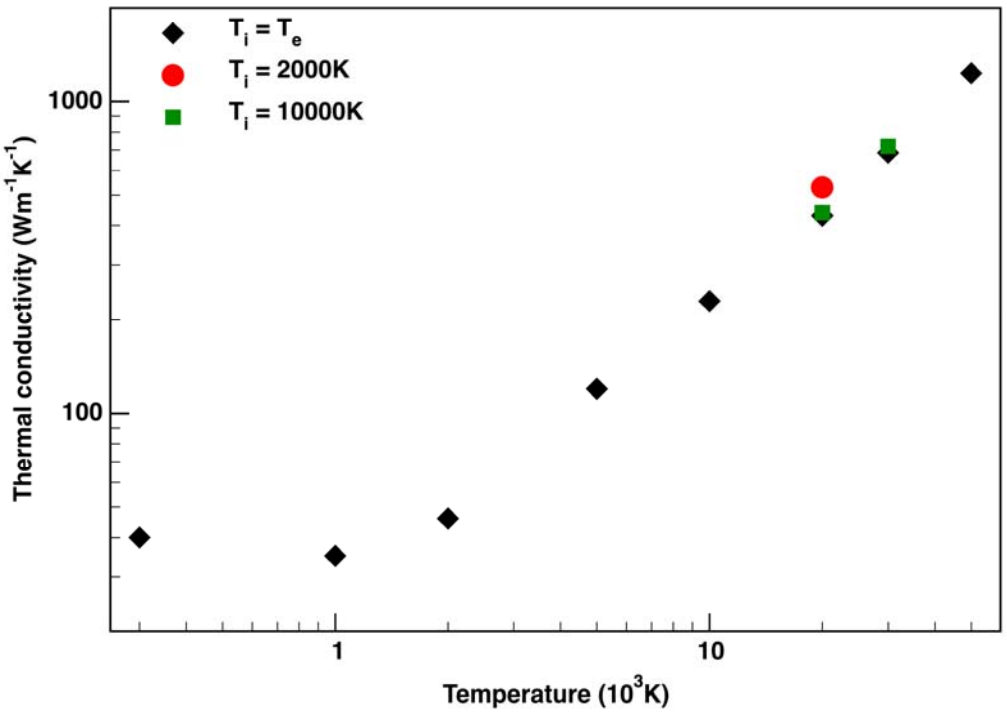

Figure 3: ab-initio thermal conductivity calculated for electron-ion non-equilibrium conditions (T_e is different from T_i) and compared to equilibrium results. T_i=2000K and T_e=20000K (solid circle), T_i=10000K and T_e=20000K (solid square), T_i=10000K and T_e=30000K (solid square).

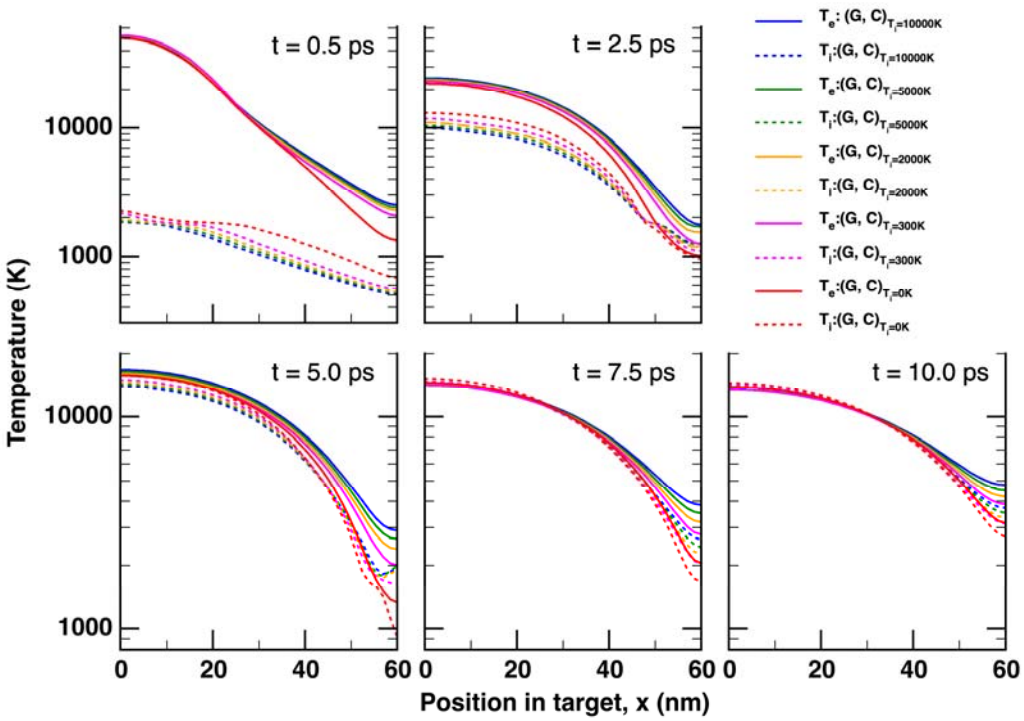

Figure 4: time evolution of electron (solid lines) and ion (dashed lines) temperature at selected delay times, t=0.5 ps, 2.5 ps, 5.0 ps, 7.5 ps and 10.0 ps calculated with several sets of thermophysical parameters (details in the text).

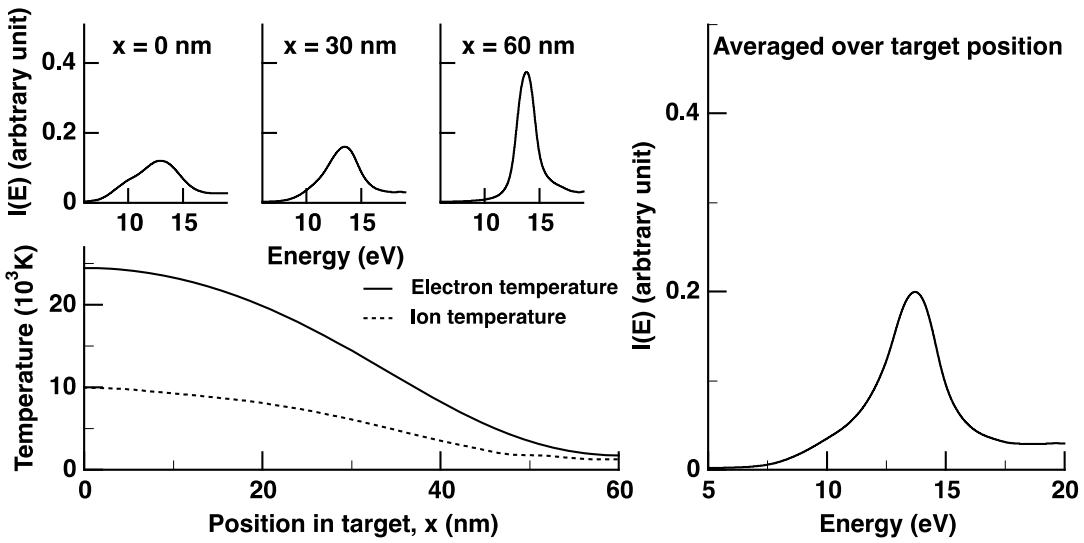

Figure 5: Electron (solid line) and ion (dashed line) temperature distribution (lower left), XANES at different target positions, x=0 nm, 30 nm, and 60 nm (upper left) and the averaged XANES (right) calculated at the delay time, t = 2.5 ps. The averaged XANES spectrum was obtained by integrating the XANES spectra calculated at the grid points spaced by 1.5 nm. The XANES spectrum at an arbitrary (T_e, T_i) values was obtained using a linear interpolation of XANES spectra self-consistently calculated on the (T_e, T_i) grid points. See text for more information about this procedure.

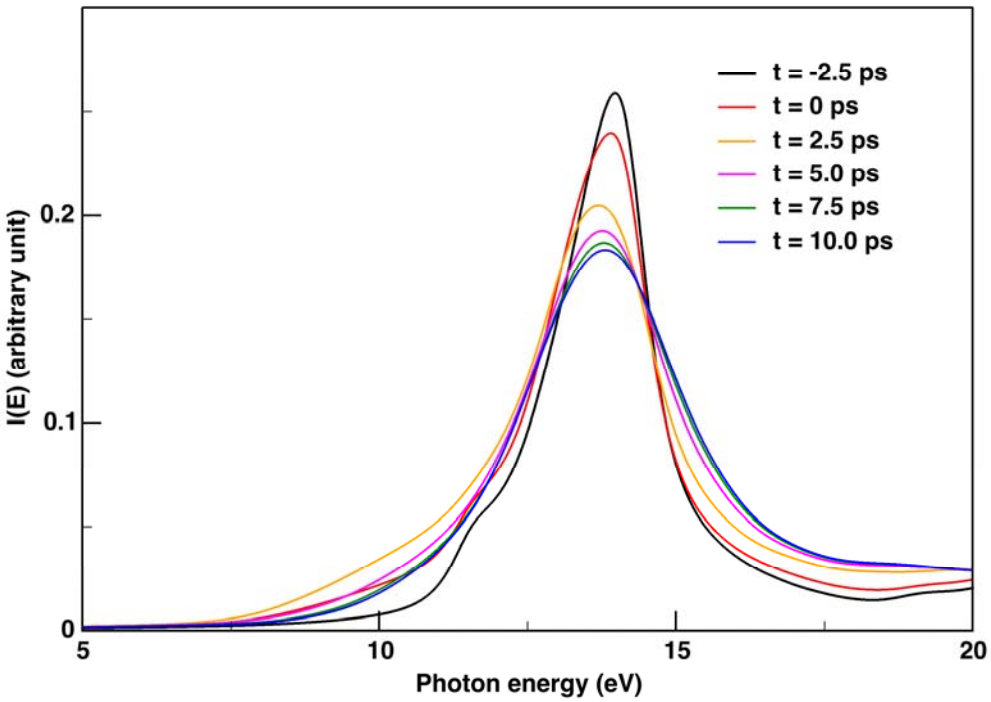

Figure 6: Time evolution of XANES calculated with $(G, C)_{Ti=10000K}$ and K_{PC}. Convolution along time axis using σ_{FWHM}=2.5ps is performed in order to reflect the experimental time resolution of about 2.5ps.

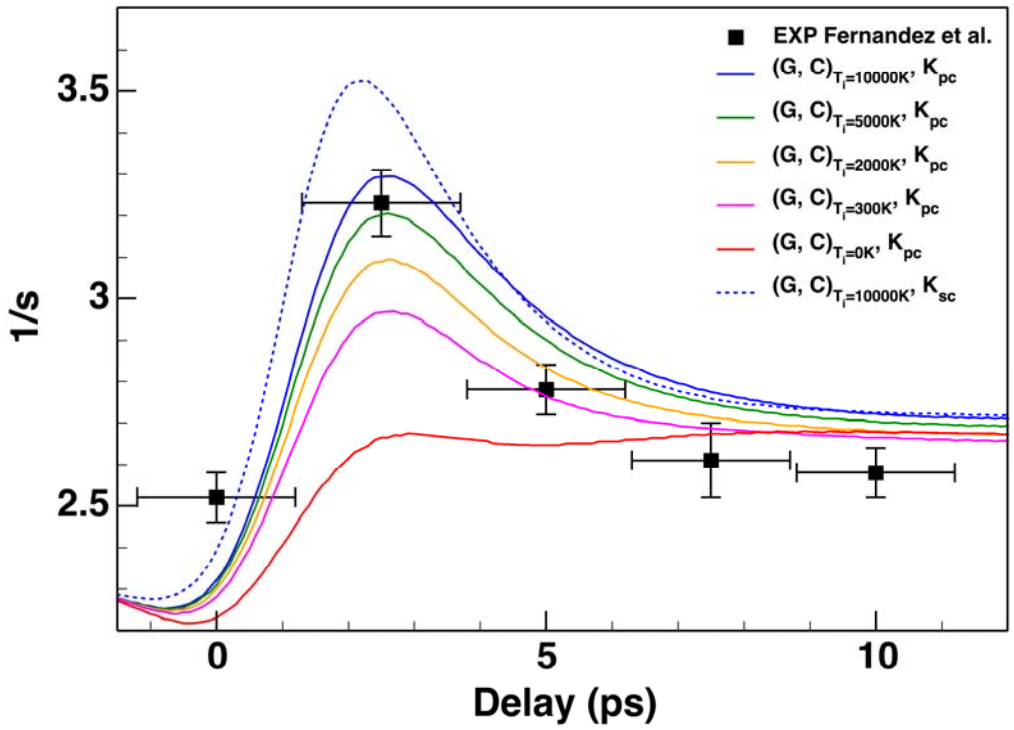

Figure 7: Simulated $1/s$ profiles for several set of (G, C, K) parameters compared with the experimental values.

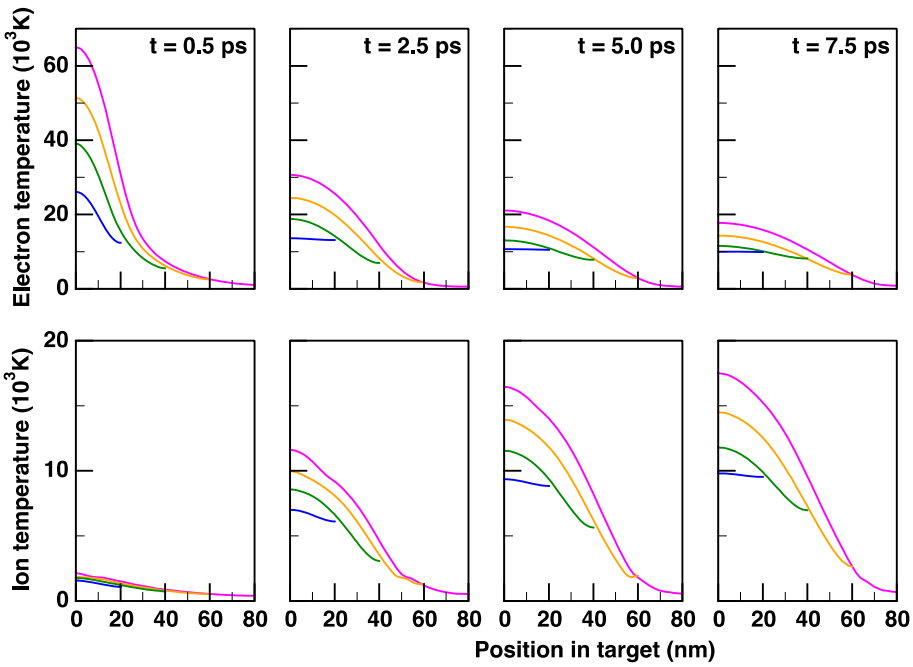

Figure 8: Time evolution of electron and ion temperatures calculated for four different target thicknesses, d=20 (blue), 40 (green), 60 (orange) and 80 nm (magenta). Upper panels are for electron temperature profiles and lower panels are for ion temperature profiles. The delay times are *t*=0.5, 2.5, 5.0, 7.5 ps. The front side electron temperature reaches to the maximum value at approximately t=0.5ps. Note the ballistic range of electrons in these TTM simulations was set at l=10nm.

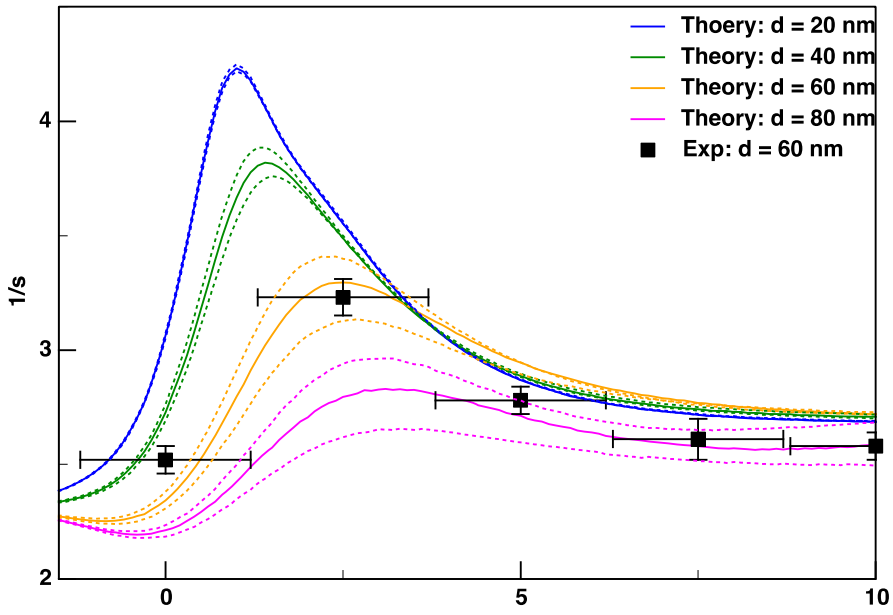

Figure 9: $1/s$ calculated with K_{PC} (solid lines) and with $K_{PC} \pm 20\%$ (dashed lines) in order to show K dependence of $1/s$. The pump laser fluences are chosen such a way that the corresponding energy densities are equivalent to that of d = 60 nm (or the value used in Ref [25]).

References:

[1] A. Ng, Int. J. Quant. Chem. **112**, 150 (2012).

[2] A. Ng, T. Ao, F. Perrot, M. W. C. Dharma-Wardana, and M. E. Foord, Laser and Particle Beams **23**, 527 (2005).

[3] M. Koenig, A. Benuzzi-Mounaix, A. Ravasio, T. Vinci, N. Ozaki, S. Lepape, D. Batani, G. Huser, T. Hall, D. Hicks, A. MacKinnon, P. Patel, H. S. Park, T. Boehly, M. Borghesi, S. Kar, and L. Romagnani, Plasma Physics and Controlled Fusion **47**, B441 (2005).

[4] R. W. Lee, S. J. Moon, H.-K. Chung, W. Rozmus, H. A. Baldis, G. Gregori, R. C. Cauble, O. L. Landen, J. S. Wark, A. Ng, S. J. Rose, C. L. Lewis, D. Riley, J.-C. Gauthier, and P. Audebert, J. Opt. Soc. Am. B **20**, 770 (2003).

[5] R. W. Lee, H. A. Baldis, R. C. Cauble, O. L. Landen, J. S. Wark, A. Ng, S. J. Rose, C. Lewis, D. Riley, J. C. Gauthier, and P. Audebert, Laser and Particle Beams **20**, 527 (2002).

[6] A. Forsman, A. Ng, G. Chiu, and R. M. More, Phys. Rev. E **58**, R1248 (1998).

[7] K. Ostrikov, F. Beg, and A. Ng, Rev. Mod. Phys. **88**, 011001 (2016).

[8] B. J. Siwick, J. R. Dwyer, R. E. Jordan, and R. J. D. Miller, Science **302**, 1382 (2003).

[9] K. Widmann, T. Ao, M. E. Foord, D. F. Price, A. D. Ellis, P. T. Springer, and A. Ng, Phys. Rev. Lett. **92**, 125002 (2004).

[10] T. Ao, Y. Ping, K. Widmann, D. F. Price, E. Lee, H. Tam, P. T. Springer, and A. Ng, Phys. Rev. Lett. **96**, 055001 (2006).

[11] Y. Ping, D. Hanson, I. Koslow, T. Ogitsu, D. Prendergast, E. Schwegler, G. Collins, and A. Ng, Phys. Rev. Lett. **96** (2006).

[12] R. Ernstorfer, M. Harb, C. T. Hebeisen, G. Sciaini, T. Dartigalongue, and R. J. D. Miller, Science **323**, 1033 (2009).

[13] J. Chen, W.-K. Chen, J. Tang, and P. M. Rentzepis, Proceedings of the National Academy of Sciences **108**, 18887 (2011).

[14] B. I. Cho, K. Engelhorn, A. A. Correa, T. Ogitsu, C. P. Weber, H. J. Lee, J. Feng, P. A. Ni, Y. Ping, A. J. Nelson, D. Prendergast, R. W. Lee, R. W. Falcone, and P. A. Heimann, Phys. Rev. Lett. **106**, 167601 (2011).

[15] Z. Chen, B. Holst, S. E. Kirkwood, V. Sametoglu, M. Reid, Y. Y. Tsui, V. Recoules, and A. Ng, Phys. Rev. Lett. **110**, 135001 (2013).

[16] B. Cho, T. Ogitsu, K. Engelhorn, A. Correa, Y. Ping, J. Lee, L. Bae, D. Prendergast, R. Falcone, and P. Heimann, Sci. Rep. **6**, 18843 (2016).

[17] S. Mazevet, Cl, eacute, J. rouin, V. Recoules, P. M. Anglade, and G. Zerah, Phys. Rev. Lett. **95**, 085002 (2005).

[18] F. Dorchies, F. Festa, V. Recoules, O. Peyrusse, A. Benuzzi-Mounaix, E. Brambrink, A. Levy, A. Ravasio, M. Koenig, T. Hall, and S. Mazevet, Phys. Rev. B **92**, 085117 (2015).

[19] V. Recoules and S. Mazevet, Phys. Rev. B **80**, 064110 (2009).

[20] S. I. Anisimov, Kapeliov.Bl, and T. L. Perelman, Zhurnal Eksperimentalnoi I Teoreticheskoi Fiziki **66**, 776 (1974).

[21] X. Y. Wang, D. M. Riffe, Y. S. Lee, and M. C. Downer, Phys. Rev. B **50**, 8016 (1994).

[22] Z. Lin, L. V. Zhigilei, and V. Celli, Phys. Rev. B **77** (2008).

[23] V. Recoules, J. Clérouin, G. Zérah, P. M. Anglade, and S. Mazevet, Phys. Rev. Lett. **96**, 055503 (2006).

[24] B. Holst, V. Recoules, S. Mazevet, M. Torrent, A. Ng, Z. Chen, S. E. Kirkwood, V. Sametoglu, M. Reid, and Y. Y. Tsui, Phys Rev B **90**, 035121 (2014).

[25] A. Fernandez-Panella, T. Ogitsu, K. Engelhorn, A. A. Correa, B. Barbrel, S. Hamel, D. Prendergast, D. Pemmaraju, M. A. Beckwith, D. Kraus, L. Jin, J. Wong, B. I. Cho, P. A. Heimann, R. W. Falcone, G. W. Collins, and Y. Ping, under review.
[26] V. Recoules and J.-P. Crocombette, Phys. Rev. B **72**, 104202 (2005).
[27] M. Pozzo, M. P. Desjarlais, and D. Alfè, Phys. Rev. B **84**, 054203 (2011).
[28] N. de Koker, G. Steinle-Neumann, and V. Vlček, Proc. Nat. Acad. Sci. **109**, 4070 (2012).
[29] A. J. Schellekens, W. Verhoeven, T. N. Vader, and B. Koopmans, App. Phys. Lett. **102** (2013).
[30] B. Y. Mueller, A. Baral, S. Vollmar, M. Cinchetti, M. Aeschlimann, H. C. Schneider, and B. Rethfeld, Phys. Rev. Lett. **111**, 167204 (2013).
[31] A. Eschenlohr, M. Battiato, P. Maldonado, N. Pontius, T. Kachel, K. Holldack, R. Mitzner, A. Föhlisch, P. M. Oppeneer, and C. Stamm, Nat. Mater. **12**, 332 (2013).
[32] D. Rudolf, C. La-O-Vorakiat, M. Battiato, R. Adam, J. M. Shaw, E. Turgut, P. Maldonado, S. Mathias, P. Grychtol, H. T. Nembach, T. J. Silva, M. Aeschlimann, H. C. Kapteyn, M. M. Murnane, C. M. Schneider, and P. M. Oppeneer, Nat. Comm. **3**, 1037 (2012).
[33] T. Roth, A. J. Schellekens, S. Alebrand, O. Schmitt, D. Steil, B. Koopmans, M. Cinchetti, and M. Aeschlimann, Phys. Rev. X **2**, 021006 (2012).
[34] M. Battiato, K. Carva, and P. M. Oppeneer, Phys. Rev. B **86**, 024404 (2012).
[35] M. Wietstruk, A. Melnikov, C. Stamm, T. Kachel, N. Pontius, M. Sultan, C. Gahl, M. Weinelt, H. A. Dürr, and U. Bovensiepen, Phys. Rev. Lett. **106**, 127401 (2011).
[36] K. Carva, M. Battiato, and P. M. Oppeneer, Phys. Rev. Lett. **107**, 207201 (2011).
[37] B. Koopmans, G. Malinowski, F. Dalla Longa, D. Steiauf, M. Fahnle, T. Roth, M. Cinchetti, and M. Aeschlimann, Nat. Mater. **9**, 259 (2010).
[38] A. Kirilyuk, A. V. Kimel, and T. Rasing, Reviews of Modern Physics **82**, 2731 (2010).
[39] M. Battiato, K. Carva, and P. M. Oppeneer, Phys. Rev. Lett. **105**, 027203 (2010).
[40] U. Atxitia, O. Chubykalo-Fesenko, J. Walowski, A. Mann, and M. Münzenberg, Phys. Rev. B **81**, 174401 (2010).
[41] J.-Y. Bigot, M. Vomir, and E. Beaurepaire, Nat. Phys. **5**, 515 (2009).
[42] E. Carpene, E. Mancini, C. Dallera, M. Brenna, E. Puppin, and S. De Silvestri, Phys. Rev. B **78**, 174422 (2008).
[43] C. Stamm, T. Kachel, N. Pontius, R. Mitzner, T. Quast, K. Holldack, S. Khan, C. Lupulescu, E. Aziz, and M. Wietstruk, Nat. Mat. **6**, 740 (2007).
[44] B. Koopmans, M. van Kampen, J. T. Kohlhepp, and W. J. M. de Jonge, Phys. Rev. Lett. **85**, 844 (2000).
[45] B. Koopmans, M. van Kampen, J. T. Kohlhepp, and W. J. M. de Jonge, J. App. Phys. **87**, 5070 (2000).
[46] J. Güdde, U. Conrad, V. Jähnke, J. Hohlfeld, and E. Matthias, Phys. Rev. B **59**, R6608 (1999).
[47] J. Hohlfeld, E. Matthias, R. Knorren, and K. H. Bennemann, Phys. Rev. Lett. **78**, 4861 (1997).
[48] E. Beaurepaire, J. C. Merle, A. Daunois, and J. Y. Bigot, Phys. Rev. Lett. **76**, 4250 (1996).
[49] P. B. Allen, Phys. Rev. Lett. **59**, 1460 (1987).
[50] L. Onsager, Phys. Rev. **37**, 405 (1931).
[51] G. V. Chester and A. Thellung, Proc. Phys. Soc. **77**, 1005 (1961).

[52] S. Mazevet, M. Torrent, V. Recoules, and F. Jollet, High Ener. Den. Phys. **6**, 84 (2010).
[53] I. S. Grigoriev and E. Z. Meilikhov, *Handbook of Physical Quantities* (CRC Press, Boca Raton, FL, 1997).
[54] Y. S. Touloukian, R. W. Powell, Ho, C. Y., and P. G. Klemens, *Thermal Conductivity-Metal Elements and Alloys* (IFI/Plenum, New York, 1971).
[55] N. W. Ashcroft and N. D. Mermin, in *Solid State Physics*: Solid State Physics. (Brooks/Cole, 10 Davis Drive Belmont, CA 94002-3098, USA, 1976), p. 499.
[56] N. Yoshikatsu, Jap. J. App. Phys. **9**, 1326 (1970).
[57] A. F. Mayadas and M. Shatzkes, Phys. Rev. B **1**, 1382 (1970).
[58] A. F. Mayadas, M. Shatzkes, and J. F. Janak, App. Phys. Lett. **14**, 345 (1969).
[59] E. H. Sondheimer, Adv. Phys. **1**, 1 (1952).
[60] W. Steinhögl, G. Schindler, G. Steinlesberger, and M. Engelhardt, Phys. Rev. B **66**, 075414 (2002).
[61] B. Feng, Z. Li, and X. Zhang, Thin Solid Films **517**, 2803 (2009).
[62] Q. G. Zhang, B. Y. Cao, X. Zhang, M. Fujii, and K. Takahashi, Phys. Rev. B **74**, 134109 (2006).
[63] J.-P. Bourgoin, G.-G. Allogho, and A. Haché, J. App. Phys. **108**, 073520 (2010).
[64] H.-D. Wang, J.-H. Liu, X. Zhang, Z.-Y. Guo, and K. Takahashi, Heat and Mass Transfer **47**, 893 (2011).
[65] Z. Xin, S. Xiaohui, Z. Xiao-Guang, and Z. Dianlin, Europhys. Lett. **96**, 17010 (2011).
[66] Q. G. Zhang, X. Zhang, B. Y. Cao, M. Fujii, K. Takahashi, and T. Ikuta, App. Phys. Lett. **89**, 114102 (2006).
[67] S. Yoneoka, J. Lee, M. Liger, G. Yama, T. Kodama, M. Gunji, J. Provine, R. T. Howe, K. E. Goodson, and T. W. Kenny, Nano Lett. **12**, 683 (2012).
[68] M. N. Ou, T. J. Yang, S. R. Harutyunyan, Y. Y. Chen, C. D. Chen, and S. J. Lai, App. Phys. Lett. **92**, 063101 (2008).
[69] H. J. Cho, S. Wang, Y. Zhou, G. Palumbo, and U. Erb, International Journal of Heat and Mass Transfer **100**, 490 (2016).
[70] H. Lin, S. Xu, X. Wang, and N. Mei, Small **9**, 2585 (2013).
[71] V. P. Zhukov, E. V. Chulkov, and P. M. Echenique, Phys. Rev. B **73**, 125105 (2006).
[72] E. V. Chulkov, A. G. Borisov, J. P. Gauyacq, D. Sánchez-Portal, V. M. Silkin, V. P. Zhukov, and P. M. Echenique, Chem. Rev. **106**, 4160 (2006).
[73] S. van Dijken, X. Jiang, and S. S. P. Parkin, Phys. Rev. B **66**, 094417 (2002).
[74] S. Arajs, B. F. Oliver, and J. T. Michalak, J. App. Phys. **38**, 1676 (1967).
[75] G. Paolo, B. Stefano, B. Nicola, C. Matteo, C. Roberto, C. Carlo, C. Davide, L. C. Guido, C. Matteo, D. Ismaila, C. Andrea Dal, G. Stefano de, F. Stefano, F. Guido, G. Ralph, G. Uwe, G. Christos, K. Anton, L. Michele, M.-S. Layla, M. Nicola, M. Francesco, M. Riccardo, P. Stefano, P. Alfredo, P. Lorenzo, S. Carlo, S. Sandro, S. Gabriele, P. S. Ari, S. Alexander, U. Paolo, and M. W. Renata, J. Phys.: Cond. Matt. **21**, 395502 (2009).
[76] J. P. Perdew, K. Burke, and M. Ernzerhof, Phys. Rev. Lett. **77**, 3865 (1996).
[77] D. Prendergast and G. Galli, Phys. Rev. Lett. **96**, 215502 (2006).
[78] D. Prendergast and S. G. Louie, Phys. Rev. B **80**, 235126 (2009).
[79] J. E. Muller, O. Jepsen, and J. W. Wilkins, Solid State Comm. **42**, 365 (1982).
[80] J. C. Fuggle and S. F. Alvarado, Phys. Rev. A **22**, 1615 (1980).
[81] I. Lindau and W. E. Spicer, Journal of Electron Spectroscopy and Related Phenomena **3**, 409 (1974).

[82] E. Pehlke and M. Scheffler, Phys. Rev. Lett. **71**, 2338 (1993).
[83] O. Peyrusse, High Ener. Den. Phys. **6**, 357 (2010).
[84] R. Nemausat, D. Cabaret, C. Gervais, C. Brouder, N. Trcera, A. Bordage, I. Errea, and F. Mauri, Phys. Rev. B **92**, 144310 (2015).
[85] V. Recoules, J. Clerouin, G. Zerah, P. M. Anglade, and S. Mazevet, Phys. Rev. Lett. **96**, 055503 (2006).
[86] T. Ogitsu, L. X. Benedict, E. Schwegler, E. W. Draeger, and D. Prendergast, Phys. Rev. B **80**, 214105 (2009).
[87] W. S. Fann, R. Storz, H. W. K. Tom, and J. Bokor, Phys. Rev. B **46**, 13592 (1992).
[88] W. S. Fann, R. Storz, H. W. K. Tom, and J. Bokor, Phys. Rev. Lett. **68**, 2834 (1992).
[89] B. Y. Mueller and B. Rethfeld, Phys. Rev. B **87**, 035139 (2013).
[90] L. Waldecker, R. Bertoni, R. Ernstorfer, and J. Vorberger, Phys. Rev. X **6**, 021003 (2016).
[91] S. Sascha, L. Wenxi, and H. Z. Ahmed, New J. Phys. **13**, 063030 (2011).
[92] R. P. Chatelain, V. R. Morrison, B. L. M. Klarenaar, and B. J. Siwick, Phys. Rev. Lett. **113**, 235502 (2014).
[93] K. Sokolowski-Tinten, C. Blome, J. Blums, A. Cavalleri, C. Dietrich, A. Tarasevitch, I. Uschmann, E. Forster, M. Kammler, M. Horn-von-Hoegen, and D. von der Linde, Nature **422**, 287 (2003).
[94] E. S. Zijlstra, L. L. Tatarinova, and M. E. Garcia, Phys. Rev. B **74**, 220301 (2006).
[95] T. G. White, J. Vorberger, C. R. D. Brown, B. J. B. Crowley, P. Davis, S. H. Glenzer, J. W. O. Harris, D. C. Hochhaus, S. Le Pape, T. Ma, C. D. Murphy, P. Neumayer, L. K. Pattison, S. Richardson, D. O. Gericke, and G. Gregori, Sci. Rep. **2** (2012).
[96] E. D. Murray, S. Fahy, D. Prendergast, T. Ogitsu, D. M. Fritz, and D. A. Reis, Phys. Rev. B **75**, 184301 (2007).
[97] C. S. Wang, R. E. Prange, and V. Korenman, Phys. Rev. B **25**, 5766 (1982).
[98] D. C. Wallace, P. H. Sidles, and G. C. Danielson, J. App. Phys. **31**, 168 (1960).
[99] H. Hasegawa and D. G. Pettifor, Phys. Rev. Lett. **50**, 130 (1983).
[100] T. Ogitsu, Y. Ping, A. Correa, B.-i. Cho, P. Heimann, E. Schwegler, J. Cao, and G. W. Collins, High Ener. Den. Phys. **8**, 303 (2012).